

Article

Impact of Thermal and Activation Energies on Glauert Wall Jet (WJ) Heat and Mass Transfer Flows Induced by ZnO-SAE50 Nano Lubricants with Chemical Reaction: The Case of Brinkman-Extended Darcy Model

Umair Khan ^{1,2} , Aurang Zaib ³  and Anuar Ishak ^{1,*} 

¹ Department of Mathematical Sciences, Faculty of Science and Technology, Universiti Kebangsaan Malaysia UKM, Bangi 43600, Malaysia

² Department of Mathematics and Social Sciences, Sukkur IBA University, Sukkur 65200, Pakistan

³ Department of Mathematical Sciences, Federal Urdu University of Arts, Science & Technology, Karachi 75300, Pakistan

* Correspondence: anuar_mi@ukm.edu.my

Abstract: Heat transfer machinery or technology is rapidly expanding due to the need for effective cooling and heating systems in the requisite automotive, chemical, and aerospace industries. This study aims to provide a numerical solution to wall jet (WJ) flow with mass and heat transport phenomenon comprising of the colloidal mixture of SAE50 and zinc oxide nanoparticles immersed in a Brinkman-extended Darcy model. The idea of WJ flow suggested by Glauert is further discussed along with the impact of the activation energy, thermal radiation, and binary chemical reaction. The leading equations are transformed into ordinary differential equations through proper similarity variables and then worked out numerically by employing a very efficient bvp4c method. The importance of pertaining quantities is illustrated and well explained through several tables and graphs. The major results suggest that the velocity profiles decline while the temperature and concentration augment due to the higher impact of nanoparticles volume fraction. In addition, the shear stress and heat transfer rate are accelerated by rising the volume fraction of nanoparticles while the Sherwood number declines with bigger impacts of nanoparticle volume fraction. In addition, the radiation factor progresses the quantitative outcomes of the heat transfer rate.

Keywords: activation energy; nanofluid; thermal radiation; Darcy-Brinkman model



Citation: Khan, U.; Zaib, A.; Ishak, A. Impact of Thermal and Activation Energies on Glauert Wall Jet (WJ) Heat and Mass Transfer Flows Induced by ZnO-SAE50 Nano Lubricants with Chemical Reaction: The Case of Brinkman-Extended Darcy Model. *Lubricants* **2023**, *11*, 22. <https://doi.org/10.3390/lubricants11010022>

Received: 19 December 2022

Revised: 4 January 2023

Accepted: 4 January 2023

Published: 7 January 2023



Copyright: © 2023 by the authors. Licensee MDPI, Basel, Switzerland. This article is an open access article distributed under the terms and conditions of the Creative Commons Attribution (CC BY) license (<https://creativecommons.org/licenses/by/4.0/>).

1. Introduction

A prescribed wall jet (WJ) is one of the interesting flowing fields produced when a faster-moving liquid is injected into a thin layer close to a vital posited surface. The external or ambient fluid may be moving or still, but often at a slower speed than the jet being injected. Such flows are of interest to scientists and engineers for several applications, such as blades for gas turbines and automotive defrosters. In essence, a WJ can be considered as dual layers stream that has an outside area and an interior zone that continues by almost the point of larger velocity in the perpendicular direction. The flow pattern in the outer area most closely matches a free shear layer, while the inner part most closely reflects a wall boundary layer. The primary characteristics of these layers differ, and their interaction in a WJ results in a complex flow field.

Glauert [1] was the primary researcher to bring up and divulge the problem of a stationary impenetrable wall forming a wall jet. Astin and Wilks [2] presented novel outcomes that show the behavior of the jet-like of Falkner-Skan equation. Zaidi et al. [3] conducted comparison research on incompressible nanofluids over a wall jet by taking into account the suspension of carbon nanotubes. They talked about how a magnetic field affects heat and stream transport. Jafarimoghaddam and Pop [4] applied the model of Tiwari

and Das [5] to inspect the jet flow and features of the heat transport phenomenon of the type of decaying exponential wall. The heat transport features in a jet flow of the Glauert type were addressed by Turkyilmazoglu [6]. The condition of velocity slip was used to describe the flow analysis. By employing the Buongiorno [7] model, Jafarimoghaddam and Shafizadeh [8] computationally evaluated the WJ stream of nanofluids and explored spatial stability. The dynamics of flow and thermal properties of a WJ through a wavy surface were explained by Kumari and Kumar [9].

An essential method for heating or cooling an object is through heat transfer. The excessive heat created by a machine or system requires either increasing or dissipating for it to operate at its best. Liquid coolants have been employed to minimize the heat of equipment such as processors and in a variety of industries such as electronics and automotive. However, regular liquid coolants display low thermal conductivity. This promotes creativity and improvement in cooling technology. The use of a fluid with metal nanoparticles in it, known as nanofluid, is one of the methods that have been found to develop the heat transfer features of liquid coolants. Metal nanoparticles are added to heat transfer fluids incorporating water, ethylene glycol, and oil to improve the heat transfer efficiency of liquid coolants since metal is a sort of substance with significant thermal conductivity (TCN). Rashid et al. [10] investigated the consequences of nanoparticles with various shapes along with the irreversibility process. The results show that the lamina shape factor of nanoparticles performs better in terms of heat exchange, irreversibility production, and temperature dispersion. The impression of stagnation-point radiative flow induced by Casson nanofluid towards a radial surface was inspected by Narender et al. [11]. The outcomes demonstrated that the rate of heat transport coefficient is augmented and the irregular radiation parameter is raised in a Casson nanofluid. Yahya et al. [12] examined the thermal characteristics of radiative flow induced by Williamson Sutterby nanofluid via a Darcy-Forchheimer spongy medium over an infinite heated plate taking into account the Cattaneo-Christov impact. Garia et al. [13] scrutinized the steady magnetohydrodynamic flow of water-based hybrid nanofluid past cone and wedge geometries with Cattaneo-Christov heat flux. Laila and Marwat [14] investigated the nanofluid flow in diverging and converging channels in the presence of inclined and heated plane walls and presented an exact solution in a limited range of physical parameters. Yaseen et al. [15] explored the features of magneto-radiative hybrid nanofluids between rotating and shrinking disks with Cattaneo-Christov heat flux. Mabood et al. [16] inspected the features of nanofluid flow through an irregular thickened stretching sheet with non-Flick's mass and non-Fourier heat fluxes. The features of a hybrid nanofluid through a shrinking/stretching sheet in a Darcy-Forchheimer porous medium were inspected by Yaseen et al. [17]. Lately, Khan et al. [18] operated the single-phase model to inspect the nanoparticle flow induced by an erratic movable sheet with convective boundary conditions. They presented double solutions in a specific domain of the movable parameter.

Activation energy is widely considered while studying a variety of physical problems, including engineering and oil storage. In addition, the field of fluid dynamics has engrossed the devotion of researchers owing to the plentiful applications of a chemical reaction and Arrhenius activation energy (AAE). At the most fundamental level, activation energy only initiates a chemical reaction. This is because even merely starting certain chemical reactions requires energy. Other uses for activation energy include compound creation, atomic processes, and the restoration of thermal lubricants. The least amount of energy required to stimulate the particles or molecules in which physical transit occurs is known as activation energy. Arrhenius defined AE in 1889. Bestman [19] reported the primary article on AAE within binary chemical reactions. Abbas et al. [20] inspected the unsteady Casson fluid flow through a movable sheet with the features of activation energy and radiation. Hsiao [21] inspected the viscous MHD flow that experiences to increase in the extrusion system's economic efficacy in the prevailing environment. Khan et al. [22] investigated the impression of AAE through a cross fluid under the movable wedge and presented double solutions. Ullah et al. [23] explored the impact of irregular thermal conductivity and

temperature-dependent viscosity on the fluid flow of nanofluid through a rotating system between parallel plates. Yesodha et al. [24] emphasized the significance of nanofluid flow with reactants chemically from a permeable stretchable sheet with activation energy.

Inertia effects and barriers in the requisite posited porous media (PM), which could modify patterns of the given dynamics flow with features of heat transport phenomenon, are disregarded by Darcy's model. It is indeed critical to determine the scenarios under which these effects apply. The model of Brinkman [25], which is an expansion of Darcy's law, had better be used for no-slip circumstances, according to Hong et al. [26]. Ishak et al. [27] utilized this model to investigate the continuous flow across a vertical experiencing object (VEO) in a PM near the stagnation point through the wall temperature. Pantokratoras [28] investigated the forced convection flow and characteristics of the heat transport phenomenon through a heated plane surface soaked in a Darcy-Brinkman porous medium (DBPM). The dissipative effect on the slip flow immersed in a DBPM was lately studied by Kausar et al. [29]. Recently, Wang [30] reported the flow via a smooth channel in a Darcy-Brinkman porous medium.

The literature reviews described above demonstrated that no attempt has been undertaken to date to inspect the Glauert jet wall flow in ZnO-SAE50 nanofluids in a Darcy-Brinkman porous media including activation energy. In addition, most applications make use of turbulent jet flow. However, the turbulent state necessitates a changeable position for the transitions in cooling applications. The nanofluid has further applications related to combustion and works well for cooling in environments with a wide temperature range. Thus, in the existing problem, the consequence of AAE on the Glauert WJ flow in a DBPM within ZnO-SAE50 nanoparticles is explored numerically. The flow problem is modeled in the form of partial differential equations. The Glauert variables are utilized to change these into ordinary differential equations (ODEs) and then numerically examined via a bvp4c solver. More intriguing variables' behavior is represented graphically.

2. Materials and Methods

The schematic pattern of the Glauert model is shown in Figure 1, where a 2D wall jet flow with mass and heat transport phenomenon involving SAE50-based fluid with ZnO nanoparticles saturated in a DBPM extended model with the important impact of mass transpiration and thermal energy effect is examined. Moreover, AAE and binary chemical reaction influences are also added to the present scrutiny. The x -axis and y -axis coordinates are taken along the corresponding horizontal surface and vertical or perpendicular to it. The liquid temperature is indicated by T , with the fixed wall temperature by T_w and the external or ambient temperature by T_∞ . Assume further, C_w and C_∞ stand for the fluid's uniform wall and ambient concentrations, respectively. However, the thermal radiation term is involved in the equation of the energy and is symbolically indicated as q_r . These presumptions allow the formation of the following leading equations [3,6]:

$$\frac{\partial u}{\partial x} + \frac{\partial v}{\partial y} = 0, \quad (1)$$

$$u \frac{\partial u}{\partial x} + v \frac{\partial u}{\partial y} = \frac{\mu_{eff} \varepsilon_a^2}{\rho_{nf}} \left(\frac{\partial^2 u}{\partial y^2} \right) - \frac{\mu_{nf} \varepsilon_a^2}{K(x) \rho_{nf}} u, \quad (2)$$

$$u \frac{\partial T}{\partial x} + v \frac{\partial T}{\partial y} = \frac{k_{nf}}{(\rho c_p)_{nf}} \left(\frac{\partial^2 T}{\partial y^2} \right) - \frac{1}{(\rho c_p)_{nf}} \frac{\partial q_r}{\partial y}, \quad (3)$$

$$q_r = \left(-\frac{4\sigma^*}{3k^*} \right) \frac{\partial T^4}{\partial y}, \quad T^4 \approx 4T_\infty^3 T - 3T_\infty^4,$$

$$u \frac{\partial C}{\partial x} + v \frac{\partial C}{\partial y} = D_f \frac{\partial^2 C}{\partial y^2} - k_r^2(x) \left(\frac{T}{T_\infty} \right)^m e^{\frac{-E_0}{k_f T}} (C - C_\infty), \quad (4)$$

along with the boundary conditions (BCs),

$$\left. \begin{aligned} u = 0, v = v_w(x), T = T_w, C = C_w \quad \text{at } y = 0, \\ u \rightarrow 0, T \rightarrow T_\infty, C \rightarrow C_\infty \quad \text{as } y \rightarrow \infty. \end{aligned} \right\} \quad (5)$$

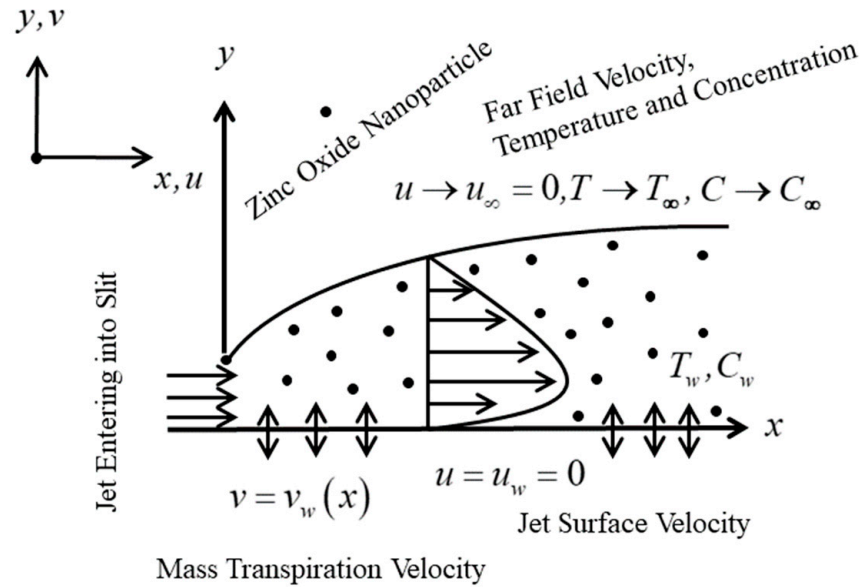


Figure 1. The geometry of the jet flow model.

Here, u and v signify the elements of velocity in the respective x - and y -axes, μ_{eff} the effective dynamic viscosity, ε_a the porosity parameter, $K(x)$ the variable permeability parameter. The mass transpiration velocity is further supposed in the form as $v_w(x) = -\sqrt{\alpha_f}x^{-3/4}f_w$, where α_f and f_w describe the thermal diffusivity and the mass suction/injection, respectively. In addition, σ^* , k^* , $k_r^2(x)$, E_a , and D_f indicate the Stefan Boltzmann constant, the mean absorption constant, the rate of variable chemical reaction, the activation energy, and the mass diffusion coefficient.

In the aforementioned stated equations, the thermal conductivity, the density, the specific heat capacity, and the dynamic viscosity of the nanofluid are symbolically denoted by k_{nf} , ρ_{nf} , $(\rho c_p)_{nf}$ and μ_{nf} , respectively. Meanwhile, the expression or correlation of the nanofluid model can be written as [6,10]:

$$\frac{k_{nf}}{k_f} = \frac{k_{snp} + 2k_f + \varphi(2k_{snp} - 2k_f)}{k_{snp} + 2k_f - \varphi(k_{snp} - k_f)}, \quad (6)$$

$$\frac{\mu_{nf}}{\mu_f} = \frac{1}{(1 - \varphi)^{2.5}}, \quad \frac{\rho_{nf}}{\rho_f} = \varphi \left(\frac{\rho_{snp}}{\rho_f} \right) + (1 - \varphi), \quad (7)$$

$$\frac{(\rho c_p)_{nf}}{(\rho c_p)_f} = \varphi \left(\frac{(\rho c_p)_{snp}}{(\rho c_p)_f} \right) + (1 - \varphi). \quad (8)$$

Therefore, Equations (6)–(8) demonstrate the physical characteristics of the ZnO-SAE50 nano-lubricants, whereas, the solid volume fraction of nanoparticles is denoted by φ . In addition, the subscript f , and snp represent the corresponding regular (viscous) fluid and the solid nanoparticles. The experimental values of physical data of the ZnO nanoparticles and ordinary base (SAE50) fluid are provided in Table 1.

Table 1. The physical properties of the nanofluid [31,32].

Nanoparticles	k (W/mK)	c_p (J/kgK)	ρ (kg/m ³)	μ (Pa s)
SAE50	0.15	1900	0.906	0.192543
ZnO	19	544	5.606	-

2.1. The Similarity Transformations

Here, we enumerated the similarity transformations listed by Glauert [1] to make it easier to examine the wall jet flow model under consideration. They are as follows:

$$\zeta = \frac{y}{\sqrt{\alpha_f}} x^{-3/4}, \psi = \sqrt{\alpha_f} x^{1/4} F(\zeta), G(\zeta) = \frac{T - T_\infty}{T_w - T_\infty}, S(\zeta) = \frac{C - C_\infty}{C_w - C_\infty} \quad (9)$$

where ψ is the requisite stream function and usually defined as $u = \partial\psi/\partial y$ and $v = -\partial\psi/\partial x$. Therefore, the velocity components can take place in the following acquired form:

$$u = \frac{4}{\sqrt{x}} F'(\zeta), \quad v = -\sqrt{\alpha_f} x^{-3/4} (F(\zeta) - 3\zeta F'(\zeta)). \quad (10)$$

2.2. The Momentum Similarity Equation

To acquire the momentum equation in a similar form, it is better to define first the variable porous medium permeability term $K(x)$ which is mathematically expressed as:

$$K(x) = K_0 \sqrt{x^3}, \quad (11)$$

where K_0 is the arbitrary positive constant.

Now using the Equations (9) and (11) in the early stated equations of this Sections 1 and 2, where the equation of continuity is satisfied and the momentum equation takes place in the form:

$$\frac{\varepsilon_b}{\rho_{nf}/\rho_f} F''' + FF'' + 2F'^2 - \frac{\mu_{nf}/\mu_f}{\rho_{nf}/\rho_f} K_a F' = 0, \quad (12)$$

where $\varepsilon_b = \frac{v_{eff}\varepsilon_a^2}{\alpha_f}$ is the modified porosity parameter.

2.3. The Energy Similarity Equation

First of all, to ease the condition of Equation (3), we substitute the approximate value of the thermal heat flux, q_r , to acquire the following form:

$$(\rho c_p)_{nf} \left(u \frac{\partial T}{\partial x} + v \frac{\partial T}{\partial y} \right) = k_f \left(\frac{k_{nf}}{k_f} + \frac{4}{3} R_d \right) \frac{\partial^2 T}{\partial y^2}, \quad (13)$$

where $R_d = \frac{4\sigma^* T_\infty^3}{k^* k_f}$ is the radiation parameter. Further, by executing Equation (9) into above stated Equation (13), one obtains:

$$\frac{1}{(\rho c_p)_{nf}/(\rho c_p)_f} \left(\frac{k_{nf}}{k_f} + \frac{4}{3} R_d \right) G'' + FG' = 0. \quad (14)$$

2.4. The Concentration Similarity Equation

For making the concentration equation a similar one, after the exercise of transformation, here, we define the reaction rate as a function of $k_r^2(x) = k_0^2 x^{-3/2}$. By utilizing Equation (9), the concentration Equation (4) yields.

$$\frac{1}{Le} S'' + FS' - \beta_a (1 + \delta_a G)^m \exp\left(\frac{-E_a}{1 + \delta_a G}\right) S = 0, \quad (15)$$

where $Le = \frac{\alpha_f}{D_f}, E_a = \frac{E_0}{k_f T_\infty}$, and $\delta_a = \frac{T_w - T_\infty}{T_\infty}$ are the Lewis number, the AAE parameter, and the temperature difference factor, respectively.

2.5. The Converted BCs

After substituting Equation (9) into Equation (5), the following transformed BCs are obtained:

$$\begin{cases} F(0) = f_w, F'(0) = 0, G(0) = S(0) = 1 \text{ at } \xi = 0, \\ F'(\xi) \rightarrow 0, G(\xi) \rightarrow 0, S(\xi) \rightarrow 0 \text{ as } \xi \rightarrow \infty. \end{cases} \tag{16}$$

Here, f_w indicates the constant mass transpiration velocity or mass suction/injection parameter. Therefore, $f_w = 0, f_w < 0$, and $f_w > 0$ signify the case of mass impermeable, injection, and suction, respectively.

2.6. The Gradients or Engineering Physical Quantities

For the considered jet problem, the following three important physical engineering quantities are used such as the friction factor C_f , the local Nusselt number Nu_x , and the local Sherwood number (mass transfer rate) Sh_x as follows:

$$\begin{aligned} C_f &= \frac{1}{\rho_f u_f^2} \left(\mu_{nf} \frac{\partial u}{\partial y} \Big|_{y=0} \right), Nu_x = \frac{x}{k_f(T_w - T_\infty)} \left(-k_{nf} \frac{\partial T}{\partial y} \Big|_{y=0} + (q_r) \Big|_{y=0} \right), \\ Sh_x &= \frac{x}{D_f(C_w - C_\infty)} \left(-D_f \frac{\partial C}{\partial y} \Big|_{y=0} \right), \end{aligned} \tag{17}$$

where the corresponding reference velocity is denoted by $u_r = 4x^{-1/2}$, see Raees et al. [33]. Further, exercising Equation (9) into the aforesaid Equation (17), we acquire,

$$2\sqrt{\frac{Re_x}{Pr}} C_f = \frac{\mu_{nf}}{\mu_f} F''(0), \frac{2Nu_x}{\sqrt{Pe_x}} = -\left(\frac{k_{nf}}{k_f} + \frac{4}{3} R_d \right) G'(0), \frac{2Sh_x}{\sqrt{Pe_x}} = -S'(0), \tag{18}$$

where $Pe_x = \frac{xu_r}{\alpha_f}$, $Re_x = \frac{xu_r}{\nu_f}$ and $Pr = \frac{\nu_f}{\alpha_f}$ are called the local Peclet number, the local Reynolds number, and the Prandtl number, respectively.

3. Numerical Methodology

The set of Equations (12), (14) and (15) along with BCs (16) are highly complicated and non-linear, which is difficult to work out, exactly or analytically. Therefore, the bvp4c scheme is implemented for the given jet problem to deal with the aforesaid similarity equations numerically. This scheme is based basically on a finite difference approach which is also further known as the three-stage Lobatto IIIA formula. In order to apply this scheme, the higher-order ODEs are changed into first-order ODEs by using the new variables as follows:

$$F = B_1, F' = B_2, F'' = B_3, G = B_4, G' = B_5, S = B_6, S' = B_7, \tag{19}$$

$$\frac{d}{d\xi} \begin{pmatrix} B_1 \\ B_2 \\ B_3 \\ B_4 \\ B_5 \\ B_6 \\ B_7 \end{pmatrix} = \begin{pmatrix} B_2 \\ B_3 \\ \frac{\rho_{nf}/\rho_f}{\epsilon_b} \left(-B_1 B_3 - 2B_2^2 + \frac{\mu_{nf}/\mu_f}{\rho_{nf}/\rho_f} K_a B_2 \right) \\ B_5 \\ \frac{(\rho c_p)_{nf}/(\rho c_p)_f}{(k_{nf}/k_f + \frac{4}{3} R_d)} (-B_1 B_5) \\ B_7 \\ Le \left(-B_1 B_7 + \beta_a (1 + \delta_a B_4)^m \exp\left(\frac{-E_a}{(1 + \delta_a B_4)} \right) B_6 \right) \end{pmatrix}, \tag{20}$$

with altered BCs are,

$$\begin{pmatrix} B_1(0) \\ B_2(0) \\ B_2(\infty) \\ B_4(0) \\ B_4(\infty) \\ B_6(0) \\ B_6(\infty) \end{pmatrix} = \begin{pmatrix} f_w \\ 0 \\ 0 \\ 1 \\ 0 \\ 1 \\ 0 \end{pmatrix}. \quad (21)$$

In order to meet the convergence criterion, the tolerance is set as $\varepsilon = 10^{-6}$, which applied throughout the computation. Since there is only one possible solution to the aforementioned jet problem, the anticipated simulation procedure desires initial or preliminary estimates to satisfy the BCs (21). For single solution problems, the initial first guess is very simple and looks obvious but in the WJ problem, it is somewhat difficult, therefore, it is better to choose the distinct influential parameter values appropriate to acquire the essential outcomes. In addition, the range is set up to $\xi_{\max} = 25$, for the considered simulations, which is pretty enough to hold or accomplished the accuracy of asymptotic convergence, see all the graphs. On the other hand, the essential part regarding the well-known accuracy, reliability, and authentication of the considered numerical code is mentioned in the form of table. Therefore, it is preferable to create a computational table, so that, we may match the original work with the available reported works for specific limiting circumstances to verify the developed code. Table 2 describes, the distinct values of the friction factor with significant impacts of φ when $f_w = 0$, $K_a = 0$ and $\varepsilon_b = 1.0$. From the tabular results, it is noticed that the single present outcome of friction factor is compared truly accurately with the reported works of Glauert [1] and Waini et al. [34]. The present and the previous works are excellently matched. Therefore, it gives us confidence that the developed code is convincing for finding the unavailable outcomes of the WJ model.

Table 2. The comparison values of shear stress $(\mu_{nf}/\mu_f)F''(0)$ for the higher impacts of φ when $\varepsilon_b = 1.00$, $K_a = 0$ and $f_w = 0$.

φ	Glauert [1]	Waini et al. [34]	Present Results
0.000	$2/9 \approx 0.2222$	0.2222	0.2222
0.035	-	-	0.3178
0.037	-	-	0.3656
0.039	-	-	0.4132

4. Analysis of Results

The discussion is based on the interpreting of the entire results for the considered WJ problem of the SAE50 plus zinc oxide nanoparticles owing to the impact of sundry distinguished parameters. The considered problem comprised of distinct factors such as the temperature difference parameter δ_a , the modified porosity parameter ε_b , the radiation parameter R_d , the solid volume fraction of nanoparticles φ , the activation parameter E_a , the dimensionless permeability parameter K_a , the chemical reaction rate parameter β_a , and the mass suction/injection parameter f_w . The consequence of these constraints on the friction factor, $(\mu_{nf}/\mu_f)F''(0)$, the Nusselt number, $-(k_{nf}/k_f + (4/3)R_d)G'(0)$, and the Sherwood number, $-S'(0)$, are quantitatively provided in Tables 3–5, respectively, whereas, the velocity $F'(\xi)$, temperature $G(\xi)$, and concentration $S(\xi)$ profiles are shown in the corresponding Figures 2–11. For the computations, we take the following default values of the constraints in the entire paper: $\varphi = 0.035$, $m = 1.0$, $K_a = 0.5$, $\varepsilon_b = 0.7$, $f_w = 1.0$, $Le = 10$, $\beta_a = 0.5$, $\delta_a = 0.5$, $E_a = 0.5$, and $R_d = 2.0$.

4.1. Research Analysis of the Tables

The quantitative results of $(\mu_{nf}/\mu_f)F''(0)$ due to variations in φ , ε_b , K_a , and f_w are illustrated in Table 3. The outcome reveals that the $(\mu_{nf}/\mu_f)F''(0)$ values escalate for larger impacts of φ , ε_b , and f_w but it shrinkages with the larger values of K_a , and, f_w . Additionally, the mass suction and blowing constraints are responsible for the biggest and smallest shear stresses that were observed in the numerical table. In contrast, the computational values of the heat transport and $-S'(0)$ of the WJ nano-lubricants are constructed quantitatively in Tables 4 and 5, respectively. Outcomes disclose that $-(k_{nf}/k_f + (4/3)R_d)G'(0)$ and $-S'(0)$ upsurge with the larger values of φ , R_d , Le , β_a , and δ_a but constant with the temperature index parameter m . However, both gradients reduce with the enormous impression of the activation parameter, and the values of φ . In addition, the largest heat transport phenomenon, and $-S'(0)$ are detected for the distinct choices of the radiation factor and Lewis number, respectively.

Table 3. The impact of $(\mu_{nf}/\mu_f)F''(0)$ for the distinct values of the sundry parameters.

φ	K_a	ε_b	f_w	Present Results
0.025	0.50	0.70	1.0	1.2781×10^{-9}
0.030	-	-	-	1.6145×10^{-9}
0.035	-	-	-	1.9234×10^{-9}
0.035	0.30	0.70	1.0	2.4134×10^{-9}
-	0.50	-	-	1.9234×10^{-9}
-	0.70	-	-	1.4560×10^{-9}
0.035	0.50	0.60	1.0	1.4477×10^{-9}
-	-	0.65	-	1.6433×10^{-9}
-	-	0.70	-	1.9234×10^{-9}
0.035	0.50	0.70	1.0	1.9234×10^{-9}
-	-	-	1.5	2.2350×10^{-7}
-	-	-	2.0	2.1850×10^{-5}
0.035	0.50	0.70	-0.05	-2.2398×10^{-8}
-	-	-	-0.10	-1.8971×10^{-8}
-	-	-	-0.15	-1.5216×10^{-8}

Table 4. The impact of $-(k_{nf}/k_f + (4/3)R_d)G'(0)$ for the distinct values of the sundry parameters.

φ	m	R_d	Present Results
0.025	1.00	2.00	1.0204154
0.030	-	-	1.0242804
0.035	-	-	1.0281458
0.035	0.00	2.00	1.0281458
-	1.00	-	1.0281458
-	2.00	-	1.0281458
0.035	1.00	1.50	1.0272708
-	-	2.00	1.0281458
-	-	2.50	1.0301780

Table 5. The impact of $-S'(0)$ for the distinct values of the sundry parameters.

φ	β_a	Le	δ_a	E_a	Present Results
0.025	0.50	10	0.50	0.50	10.5067960
0.030	-	-	-	-	10.5067950
0.035	-	-	-	-	10.5067940
0.035	0.30	10	0.50	0.50	10.3097350
-	0.50	-	-	-	10.5067940
-	0.70	-	-	-	10.6971130
0.035	0.50	7.5	0.50	0.50	7.99799500
-	-	0.90	-	-	9.50379410
-	-	10.5	-	-	11.0081000
0.035	0.50	10	0.50	0.50	10.5067940
-	-	-	1.00	-	10.5067940
-	-	-	1.50	-	10.9238810
0.035	0.50	10	0.50	0.50	10.5067940
-	-	-	-	1.00	10.3670720
-	-	-	-	1.50	10.2648640

4.2. Research Analysis of the Velocity Curve Profiles

Figures 2–4 illustrate the velocity profiles of the SAE50 plus zinc oxide nano-lubricants for the single branch solutions due to the influence of φ , K_a , and ε_b , respectively. From the tendency of the graphical outcomes, it is perceived that the curves of velocity fulfill the criterion of asymptotic convergence, and hence mathematically satisfy the appropriate BCs owing to the successive impact of the influential parameters. To make this point clearer, the results in Figure 2 show that the velocity field curves constantly decelerate as the value of φ rises. In general, the viscosity impact is improved by the solid nanoparticle volume fraction, as a result, the WJ flow velocity decreases. Alternatively, the curves of velocity primarily decelerate and then accelerate with bigger values of K_a and ε_b as elaborated in the respective Figures 3 and 4. According to the basic concept of physics, if the value of K_a rises, as a response, the value of v_f also rises. Thus, the larger viscosity of the fluid arises with the higher impact of K_a which physically slows down the speed of the WJ flow, in conclusion, the velocity $F'(\xi)$ decelerates. Similarly, following the above explanation for the modified porosity parameter, one obtains $\varepsilon_b = v_{eff}\varepsilon_a^2/\alpha_f$. Additionally, the space between the curves for larger K_a is well enough than the space that appeared in the curves for the larger consequences of ε_b .

4.3. Research Analysis of the Temperature Curve Profiles

The impacts of φ and R_d on $G(\xi)$ of the SAE50 plus zinc oxide (ZnO) nano-lubricants for the single branch solutions are exhibited in Figures 5 and 6, respectively. From the results, it is deduced that the temperature curves and the thermal boundary layer thickness (TBLT) are constantly improved with the larger influence of φ and R_d . In the physical scenario, increasing radiation results in the release of extra energy into the wall jet flow, which leads to the development of the temperature field and the TBLT. Moreover, the gap between the curves is less in Figure 5 as compared to Figure 6 due to the larger values of φ and R_d .

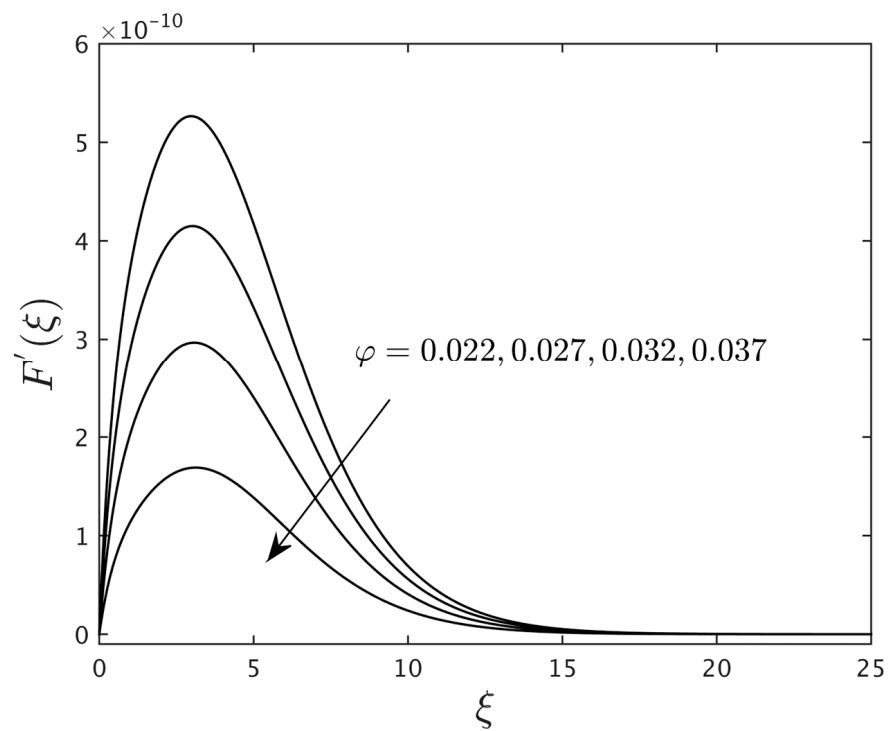


Figure 2. The velocity profiles $F'(\xi)$ for the change values of φ when $m = 1.0$, $K_a = 0.5$, $\varepsilon_b = 0.7$, $f_w = 1.0$, $Le = 10$, $\beta_a = 0.5$, $\delta_a = 0.5$, $R_d = 2.0$, and $E_a = 0.5$.

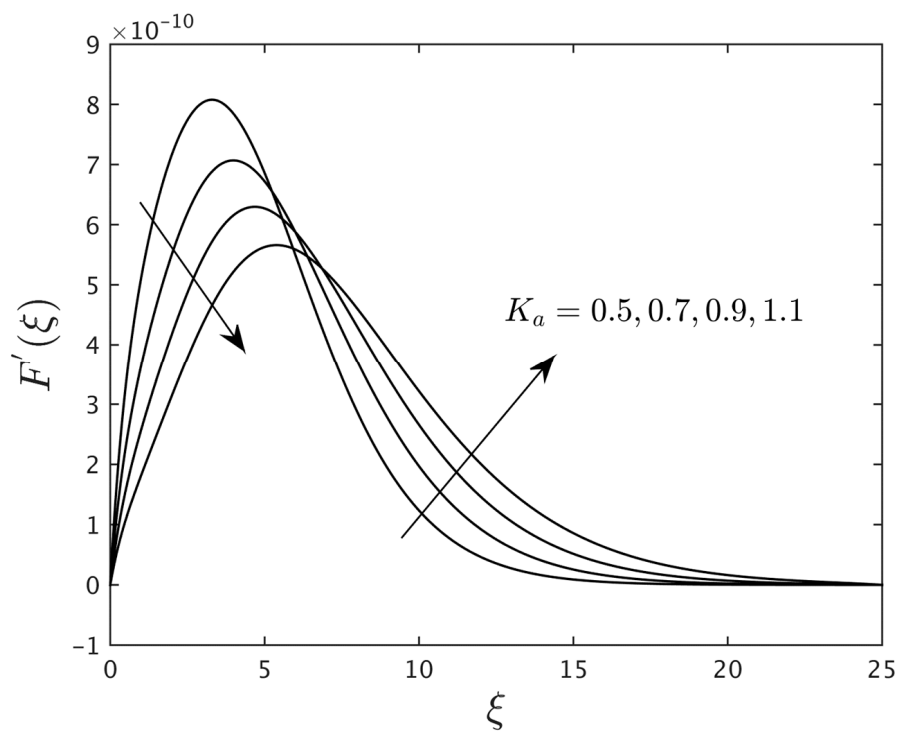


Figure 3. The velocity profiles $F'(\xi)$ for the change values of K_a when $m = 1.0$, $\varphi = 0.035$, $\varepsilon_b = 0.7$, $f_w = 1.0$, $Le = 10$, $\beta_a = 0.5$, $\delta_a = 0.5$, $E_a = 0.5$, and $R_d = 2.0$.

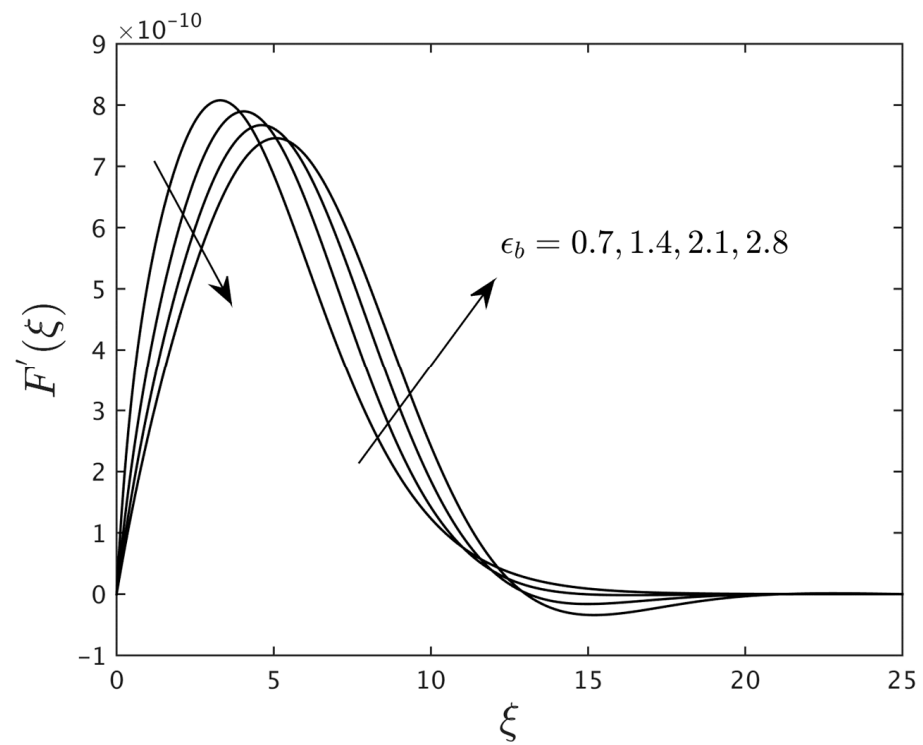


Figure 4. The velocity profiles $F'(\xi)$ for the change values of ϵ_b when $m = 1.0$, $\varphi = 0.035$, $f_w = 1.0$, $K_a = 0.5$, $Le = 10$, $\beta_a = 0.5$, $\delta_a = 0.5$, $E_a = 0.5$, and $R_d = 2.0$.

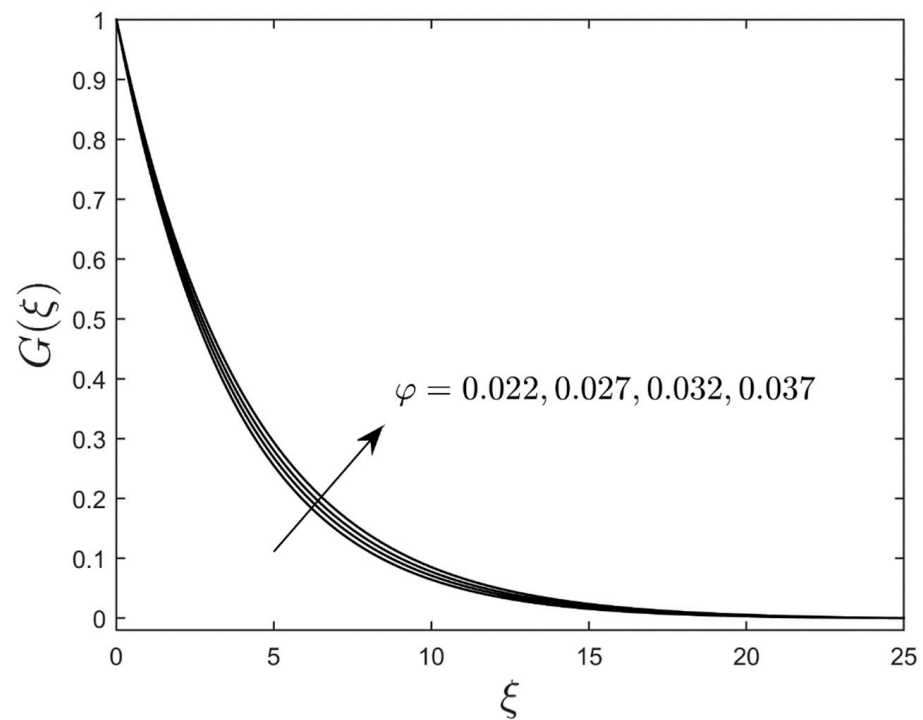


Figure 5. The temperature profiles $G(\xi)$ for the change values of φ when $m = 1.0$, $K_a = 0.5$, $\epsilon_b = 0.7$, $f_w = 1.0$, $Le = 10$, $\beta_a = 0.5$, $\delta_a = 0.5$, $R_d = 2.0$, and $E_a = 0.5$.

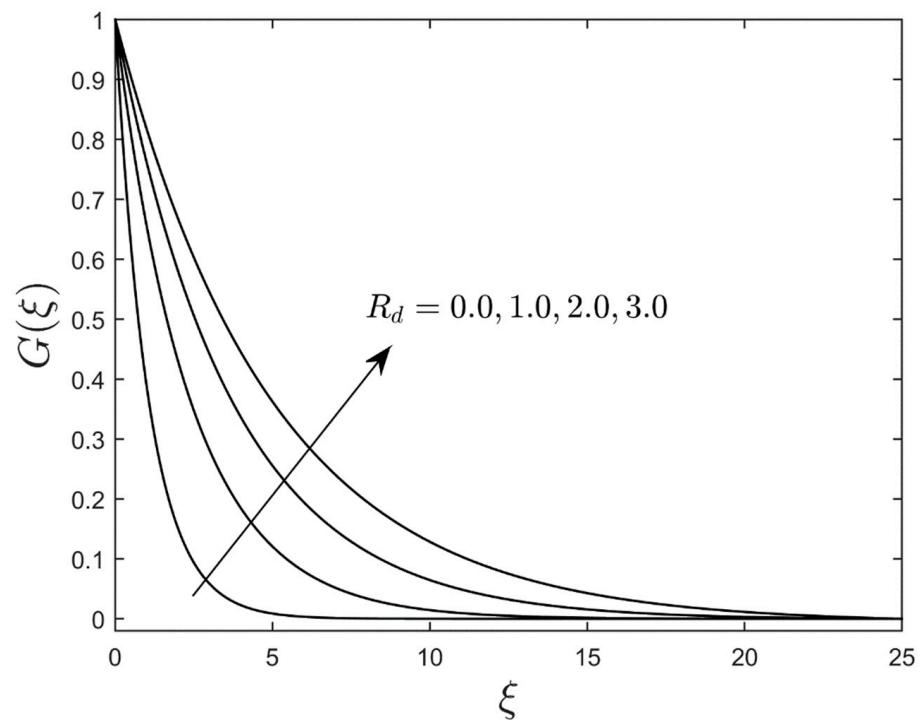


Figure 6. The temperature profiles $G(\xi)$ curves for sundry choices of R_d when $\varepsilon_b = 0.7$, $K_a = 0.5$, $f_w = 1.0$, $Le = 10$, $m = 1.0$, $\beta_a = 0.5$, $\delta_a = 0.5$, $E_a = 0.5$, and $\varphi = 0.035$.

4.4. Research Analysis of the Concentration Curve Profiles

Figures 7–11 exemplify the concentration profile $S(\xi)$ of the SAE50 plus zinc oxide nano-lubricants for the single branch results owing to the influence of φ , Le , β_a , δ_a , and E_a , respectively. In all the graphs, it is realized that the pertinent BCs are satisfied and the pattern of the outputs converges asymptotically for varying the several distinguished constraints. Moreover, Figure 7 illustrates the effect of φ on the $S(\xi)$. For a rising value of φ , the concentration profile of the wall jet flow escalates. Figures 8–11, it is evident that the upsurging values of Le , β_a and δ_a reduce the dimensionless concentration profiles of the wall jet flow, respectively, while it intensifies with the higher impacts of E_a . In Figure 8 such a pattern of solution curves happens due to the fact that the mass diffusivity of the fluid reduces with the huge effects of the Lewis number, as a result, the fluid is less concentrated at the surface of the wall jet. However, the activation and chemical reaction term $\beta_a(1 + \delta_a G)^m \exp(-E_a/1 + \delta_a G)S$ in the requisite concentration similarity equation (16) was written with the negative sign which further shows that whenever we increase the impact of β_a and δ_a , as a result, the concentration decelerates (see Figures 9 and 10). In addition, for Figure 11, this exponential term such as $\exp(-E_a/1 + \delta_a G)S$ is an exceptional tool that how the AAE disturbs $S(\xi)$. Henceforth, due to a superior impact of E_a , the thickness of the CBL and the concentration $S(\xi)$ upsurges.

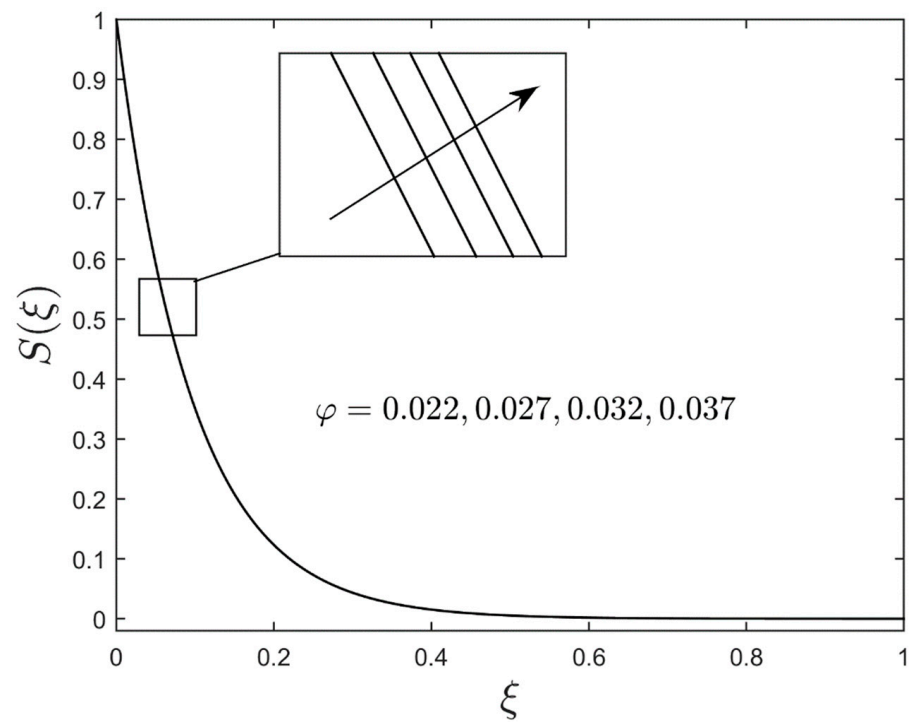


Figure 7. The concentration profiles $S(\xi)$ for the change values of φ when $m = 1.0$, $K_a = 0.5$, $\varepsilon_b = 0.7$, $f_w = 1.0$, $Le = 10$, $\beta_a = 0.5$, $\delta_a = 0.5$, $E_a = 0.5$, and $R_d = 2.0$.

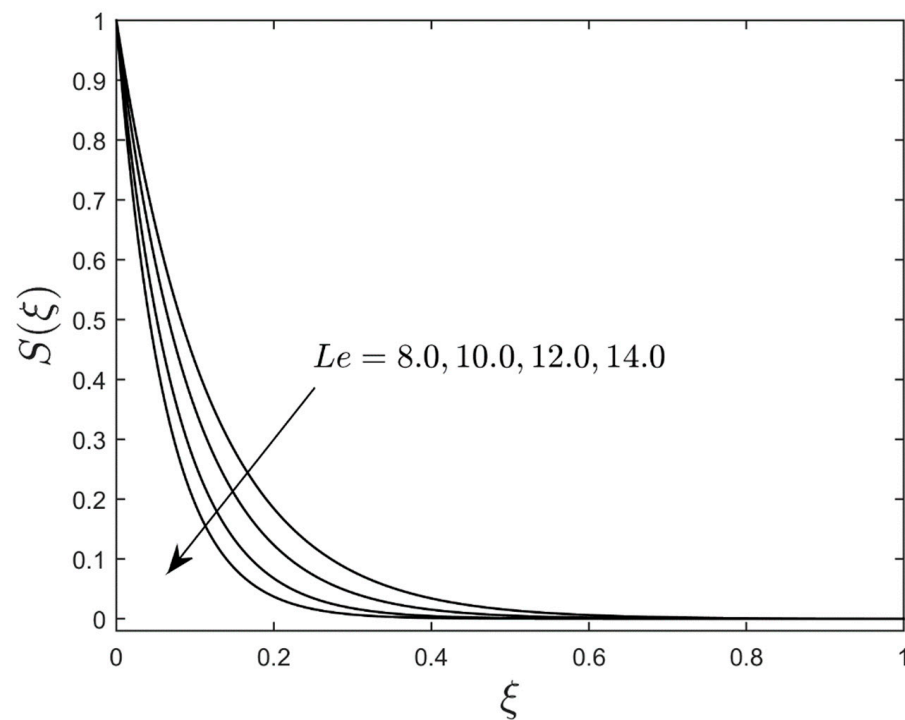


Figure 8. The concentration profiles $S(\xi)$ for the change values of Le when $m = 1.0$, $K_a = 0.5$, $\varepsilon_b = 0.7$, $f_w = 1.0$, $\varphi = 0.035$, $\beta_a = 0.5$, $\delta_a = 0.5$, $E_a = 0.5$, and $R_d = 2.0$.

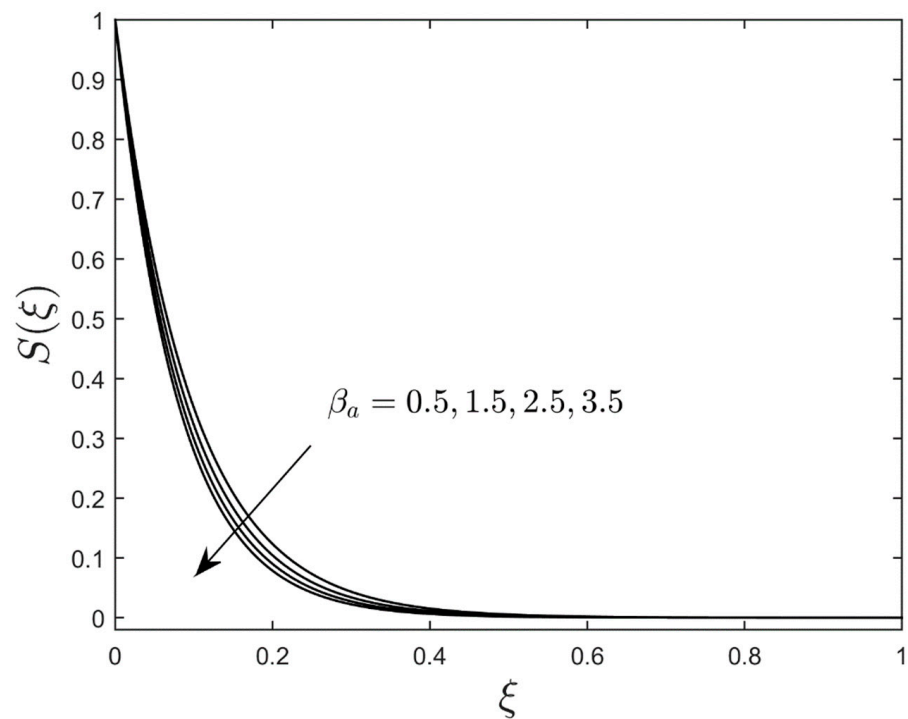


Figure 9. The concentration profiles $S(\xi)$ for the change values of β_a when $m = 1.0$, $K_a = 0.5$, $\varepsilon_b = 0.7$, $f_w = 1.0$, $Le = 10$, $\varphi = 0.035$, $\delta_a = 0.5$, $E_a = 0.5$, and $R_d = 2.0$.

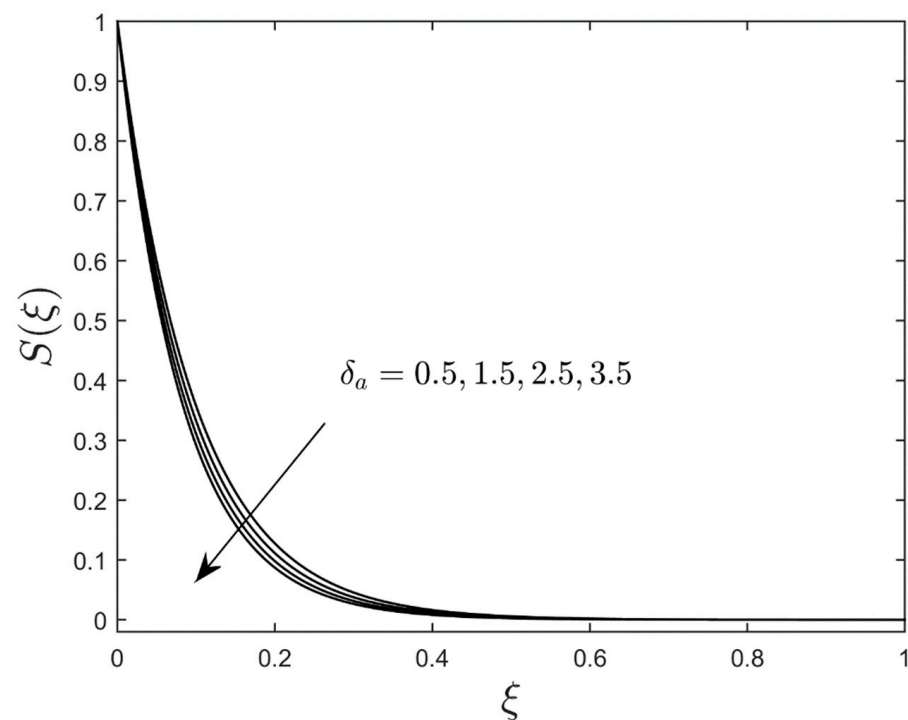


Figure 10. The concentration profiles $S(\xi)$ for the change values of δ_a when $m = 1.0$, $K_a = 0.5$, $\varepsilon_b = 0.7$, $f_w = 1.0$, $Le = 10$, $\beta_a = 0.5$, $\varphi = 0.035$, $E_a = 0.5$, and $R_d = 2.0$.

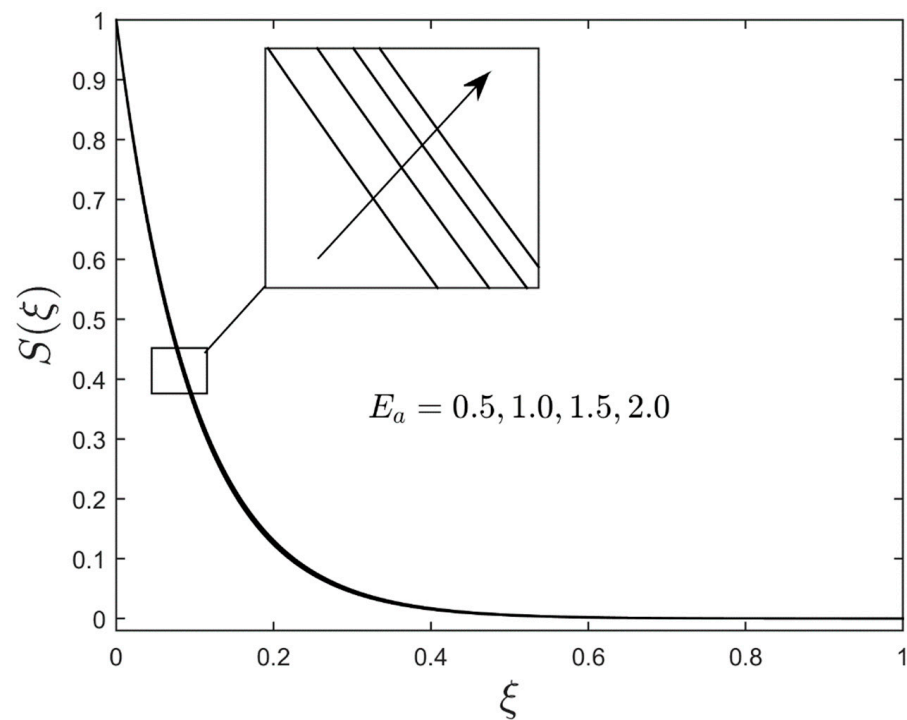


Figure 11. The concentration profiles $S(\xi)$ for the change values of E_a when $m = 1.0$, $K_a = 0.5$, $\varepsilon_b = 0.7$, $f_w = 1.0$, $Le = 10$, $\beta_a = 0.5$, $\delta_a = 0.5$, $\varphi = 0.035$, and $R_d = 2.0$.

5. Conclusions

The thermal radiative heat and mass transfer analysis of 2D WJ flows conveying SAE50-ZnO nano-lubricants with mass transpiration or suction/injection velocity, and chemical reaction has been investigated. Moreover, the AAE and the Darcy-Brinkman porous medium model are also added to the investigation. The governing equations are transformed to the set of non-linear ODEs using the Glauert WJ variables, which are then worked out computationally via the effective bvp4c scheme. The following are the main outcomes of the present study:

- The velocity curves of the WJ flow moderate with a superior impact of the nanoparticle volume fraction but the temperature and concentration profile curves are enhanced.
- The modified porosity parameter and the dimensionless permeability parameter impact initially decay the motion of the wall jet flow and then abruptly augmented the velocity.
- With the increasing value of the radiation parameter, the temperature profiles and the thickness of the thermal boundary layer developed.
- The concentration enriches with a higher impact of activation energy but shrinkages with Le , β_a and δ_a .
- The friction factor upsurges and magnitude-wise declines due to the larger impressions of the mass suction factor and mass blowing factor, respectively.
- The rate of heat transfer is boosted due to the higher influences of the nanoparticle volume fraction while the mass transfer rate decelerates.

Author Contributions: Conceptualization, U.K. and A.Z.; methodology, U.K.; software, U.K.; validation, U.K., A.Z. and A.I.; formal analysis, A.I.; investigation, A.I.; resources, A.Z.; data curation, A.Z.; writing—original draft preparation, U.K. and A.Z.; writing—review and editing, U.K., A.Z. and A.I.; visualization, A.Z.; supervision, A.I.; project administration, A.I.; funding acquisition, A.I. All authors have read and agreed to the published version of the manuscript.

Funding: Universiti Kebangsaan Malaysia (DIP-2020-001).

Data Availability Statement: Not applicable.

Conflicts of Interest: The authors declare no conflict of interest.

References

1. Glauert, M.B. The wall jet. *J. Fluid Mech.* **1956**, *1*, 625–643. [\[CrossRef\]](#)
2. Astin, P.; Wilks, G. Jet profile solutions of the Falkner-Skan equation. *Z. Angew. Math. Und Phys. ZAMP* **1996**, *47*, 790–798. [\[CrossRef\]](#)
3. Zaidi, S.Z.A.; Mohyud-Din, S.T.; Bin-Mohsen, B. A comparative study of wall jet flow containing carbon nanotubes with convective heat transfer and MHD. *Eng. Comput.* **2017**, *3*, 739–753. [\[CrossRef\]](#)
4. Jafarimoghaddam, A.; Pop, I. Numerical modeling of Glauert type exponentially decaying wall jet flows of nanofluids using Tiwari and Das' nanofluid model. *Int. J. Numer. Meth. Heat Fluid Flow* **2018**, *2*, 1010–1038. [\[CrossRef\]](#)
5. Tiwari, R.K.; Das, M.K. Heat transfer augmentation in a two-sided lid-driven differentially heated square cavity utilizing nanofluids. *Int. J. Heat Mass Transf.* **2007**, *50*, 2002–2018. [\[CrossRef\]](#)
6. Turkyilmazoglu, M. Laminar slip wall jet of Glauert type and heat transfer. *Int. J. Heat Mass Transf.* **2019**, *134*, 1153–1158. [\[CrossRef\]](#)
7. Buongiorno, J. Convective transport in nanofluids. *J. Heat Transf.* **2006**, *128*, 240–250. [\[CrossRef\]](#)
8. Jafarimoghaddam, A.; Shafizadeh, F. Numerical modeling and spatial stability analysis of the wall jet flow of nanofluids with thermophoresis and Brownian effects. *Propuls. Power Res.* **2019**, *8*, 210–220. [\[CrossRef\]](#)
9. Kumari, A.; Kumar, A. Heat transfer and fluid flow characteristics of a turbulent wall jet with a wavy wall. *Int. J. Heat Fluid Flow* **2021**, *87*, 108749. [\[CrossRef\]](#)
10. Rashid, U.; Baleanu, D.; Iqbal, A.; Abbas, M. Shape effect of nanosize particles on magnetohydrodynamic nanofluid flow and heat transfer over a stretching sheet with entropy generation. *Entropy* **2020**, *22*, 1171. [\[CrossRef\]](#)
11. Narender, G.; Govardhan, K.; Sarma, G.S. Magnetohydrodynamic stagnation point on a Casson nanofluid flow over a radially stretching sheet. *Beilstein J. Nanotechnol.* **2020**, *11*, 1303–1315. [\[CrossRef\]](#)
12. Yahya, A.U.; Salamat, N.; Habib, D.; Ali, B.; Hussain, S.; Abdal, S. Implication of bio-convection and Cattaneo–Christov heat flux on Williamson Sutterby nanofluid transportation caused by a stretching surface with convective boundary. *Chin. J. Phys.* **2021**, *73*, 706–718. [\[CrossRef\]](#)
13. Garia, R.; Rawat, S.K.; Kumar, M.; Yaseen, M. Hybrid nanofluid flow over two different geometries with Cattaneo–Christov heat flux model and heat generation: A model with correlation coefficient and probable error. *Chin. J. Phys.* **2021**, *74*, 421–439. [\[CrossRef\]](#)
14. Laila, R.; Marwat, D.N.K. Nanofluid flow in a converging and diverging channel of rectangular and heated walls. *Ain Shams Eng. J.* **2021**, *12*, 4023–4035. [\[CrossRef\]](#)
15. Yaseen, M.; Rawat, S.K.; Kumar, M. Cattaneo–Christov heat flux model in Darcy–Forchheimer radiative flow of MoS₂–SiO₂/kerosene oil between two parallel rotating disks. *J. Therm. Anal. Calorim.* **2022**, *147*, 10865–10887. [\[CrossRef\]](#)
16. Mabood, F.; Imtiaz, M.; Rafiq, M.; El-Zahar, E.R.; Sidi, M.O.; Khan, M.I. Bidirectional rotating flow of nanofluid over a variable thickened stretching sheet with non-Fourier's heat flux and non-Fick's mass flux theory. *PLoS ONE* **2022**, *17*, e0265443. [\[CrossRef\]](#)
17. Yaseen, M.; Rawat, S.K.; Kumar, M. Analysis of MoS₂–SiO₂/water hybrid nanofluid flow with linear and quadratic thermal radiation induced by a stretching/shrinking surface in a Darcy-Forchheimer porous medium. *Spec. Top. Rev. Porous Media Int. J.* **2022**, *13*, 31–48. [\[CrossRef\]](#)
18. Khan, U.; Zaib, A.; Pop, I.; Waini, I.; Ishak, A. MHD flow of a nanofluid due to a nonlinear stretching/shrinking sheet with a convective boundary condition: Tiwari–Das nanofluid model. *Int. J. Num. Meth. Heat Fluid Flow* **2022**, *32*, 3233–3258. [\[CrossRef\]](#)
19. Bestman, A.R. Natural convection boundary layer with suction and mass transfer in a porous medium. *Int. J. Energy Res.* **1990**, *14*, 389–396. [\[CrossRef\]](#)
20. Abbas, Z.; Sheikh, M.; Motsa, S.S. Numerical solution of binary chemical reaction on stagnation point flow of Casson fluid over a stretching/shrinking sheet with thermal radiation. *Energy* **2016**, *95*, 12–20. [\[CrossRef\]](#)
21. Hsiao, K.L. To promote radiation electrical MHD activation energy thermal extrusion manufacturing system efficiency by using Carreau-nanofluid with parameters control method. *Energy* **2017**, *130*, 486–499. [\[CrossRef\]](#)
22. Khan, U.; Zaib, A.; Baleanu, D.; Sheikholeslami, M.; Wakif, A. Exploration of dual solutions for an enhanced cross liquid flow past a moving wedge under the significant impacts of activation energy and chemical reaction. *Heliyon* **2020**, *6*, e04565. [\[CrossRef\]](#)
23. Ullah, I.; Alghamdi, M.; Xia, W.-F.; Shah, S.I.; Khan, H. Activation energy effect on the magnetized-nanofluid flow in a rotating system considering the exponential heat source. *Int. Commun. Heat Mass Transf.* **2021**, *128*, 105578. [\[CrossRef\]](#)
24. Yesodha, P.; Bhuvanawari, M.; Sivasankaran, S. Nanofluid flow with activation energy and heat generation under slip boundary condition with convective heat and mass transfer. *Mater. Proc.* **2022**, *59*, 959–967. [\[CrossRef\]](#)
25. Brinkman, H.C. On the permeability of media consisting of closely packed porous particles. *Appl. Sci. Res.* **1947**, *1*, 81–86. [\[CrossRef\]](#)
26. Hong, J.T.; Yamada, Y.; Tien, C.L. Effects of non-Darcian and non-uniform porosity on vertical plate natural convection in porous media. *ASME J. Heat Transf.* **1987**, *109*, 356–362. [\[CrossRef\]](#)

27. Ishak, A.; Nazar, R.; Pop, I. Dual solutions in mixed convection flow near a stagnation point on a vertical surface in a porous medium. *Int. J. Heat Mass Transf.* **2008**, *51*, 1150–1155. [[CrossRef](#)]
28. Pantokratoras, A. Forced convection in a Darcy–Brinkman porous medium with a convective thermal boundary condition. *J. Porous Media* **2015**, *18*, 873–878. [[CrossRef](#)]
29. Kausar, M.S.; Hassan, A.; Mamat, M.; Ahmad, B. Boundary layer flow through Darcy–Brinkman porous medium in the presence of slip effects and porous dissipation. *Symmetry* **2019**, *11*, 659. [[CrossRef](#)]
30. Wang, C.Y. Darcy–Brinkman flow in channels of arbitrary curvature. *J. Porous Media* **2022**, *25*, 1–10. [[CrossRef](#)]
31. Nayak, M.K.; Prakash, J.; Tripathi, D.; Pandey, V.S. 3D radiative convective flow of ZnO–SAE50 nano-lubricant in the presence of varying magnetic field and heterogeneous reaction. *Propuls. Power Res.* **2019**, *8*, 339–350. [[CrossRef](#)]
32. Avramenko, A.A.; Shevchuk, I.V. *Modelling of Convective Heat and Mass Transfer in Nanofluids with and without Boiling and Condensation*; Springer International Publishing: Cham, Switzerland, 2022.
33. Raees, A.; Hang, X.; Raees-ul-Haq, M. Explicit solutions of wall jet flow subject to a convective boundary condition. *Bound. Value Prob.* **2014**, *2014*, 163. [[CrossRef](#)]
34. Waini, I.; Ishak, A.; Pop, I. MHD Glauert flow of a hybrid nanofluid with heat transfer. *J. Adv. Res. Fluid Mech. Therm. Sci.* **2021**, *86*, 91–100. [[CrossRef](#)]

Disclaimer/Publisher’s Note: The statements, opinions and data contained in all publications are solely those of the individual author(s) and contributor(s) and not of MDPI and/or the editor(s). MDPI and/or the editor(s) disclaim responsibility for any injury to people or property resulting from any ideas, methods, instructions or products referred to in the content.